TRANSIENT SIMULATION AND PERFORMANCE ANALYSIS OF NOVEL EVAPORATOR FOR OTEC APPLICATION

Eyad Abureisha[1], Siti Norasyiqin Abdul Latif[2], Chun Mein Soon[2], Mahadhir Mohammad [2], Meng Soon Chiong[1,2]*

[1]Faculty of Mechanical Engineering, Universiti Teknologi Malaysia, 81310 UTM Johor Bahru, Johor, Malaysia
[2]Institute for Sustainable Transport, Universiti Teknologi Malaysia, 81310 UTM Johor Bahru, Johor, Malaysia

Article history
Received
1st December 2025
Received in revised form
11th December 2025
Accepted
11th December 2025
Accepted
12th December 2025

*Corresponding author
chiongms@utm.my

GRAPHICAL ABSTRACT

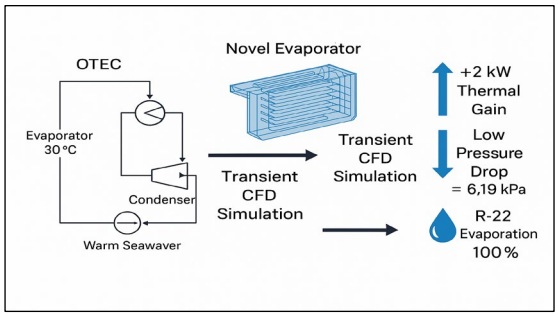

Turbulence-enhancing modifications at the inlet were identified to further accelerate phase change without excessive pressure penalties. These advancements support more efficient Rankine cycle implementations, improving OTEC feasibility and scalability. This study contributes to the development of high-performance heat exchangers, advancing OTEC as a sustainable energy solution.

ABSTRACT

Ocean Thermal Energy Conversion (OTEC) harnesses the temperature difference between warm surface seawater and cold deep seawater to generate electricity. The evaporator, a key component, facilitates heat absorption and phase change in the working fluid. This study presents a transient simulation and performance analysis of a novel evaporator design for OTEC, aiming to enhance heat transfer efficiency while minimizing pressure drop. A computational fluid dynamics (CFD) model was developed using ANSYS Fluent, incorporating various mass flow rates and turbulence models. The k-omega SST model proved most effective in capturing phase change dynamics. Results show the proposed design absorbs 2 kW more thermal energy than conventional designs at scale, with an optimal flow rate of 0.01856 kg/s balancing energy and pressure constraints. The maximum pressure drop was 6.19 kPa for R-22, significantly lower than traditional heat exchangers. The design improves heat transfer and reduces energy losses, enhancing OTEC system efficiency.

KEYWORDS

Ocean Thermal Energy Conversion; Evaporator Design; Transient CFD Simulation.

1.0 INTRODUCTION

OTEC is a renewable energy technology that generates electricity by utilizing the temperature difference between warm surface waters and deep cold ocean waters, primarily in equatorial regions where the differential exceeds 20°C year-round. A typical 100 MW OTEC facility requires 10-20 billion gallons of water daily. In a closed-cycle OTEC system, warm surface water evaporates a working fluid, such as R717 (ammonia) or R22, which drives a turbine to generate electricity. The vapor is then condensed by cold water in a secondary heat exchanger, completing the cycle. The cold-water pipe, which must extract water from depths of around 1000 meters, is a key feature of OTEC systems and presents significant engineering challenges. These systems are housed on surface platforms, connected to the power grid by cables. Beyond energy generation, OTEC facilities can support aquaculture, seawater air conditioning, and produce byproducts like

potable water, ammonia, and hydrogen [1]. Figure 1 illustrates the basic configuration of a simple Rankine cycle, consisting of the boiler (evaporator), turbine, condenser, and pump operating in a closed-loop system.

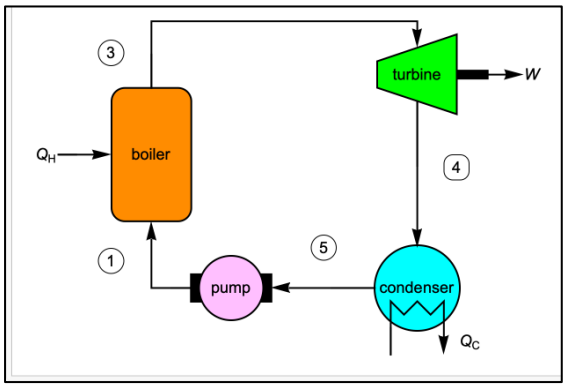

Figure 1: Simple Rankine cycle

The evaporator is a critical component of the OTEC system and performs a role analogous to boilers in conventional power plants. Because OTEC operates within a narrow temperature difference, small inefficiencies in heat transfer or excessive pressure drops can significantly reduce net power output. Conventional plate heat exchanger evaporators suffer from several limitations, including high pressure losses, gasket sealing failures, limited pressure resistance, corrosion, and biofouling in marine environments. These issues lead to increased pumping power requirements, reduced turbine inlet pressure, and lower system reliability [25].

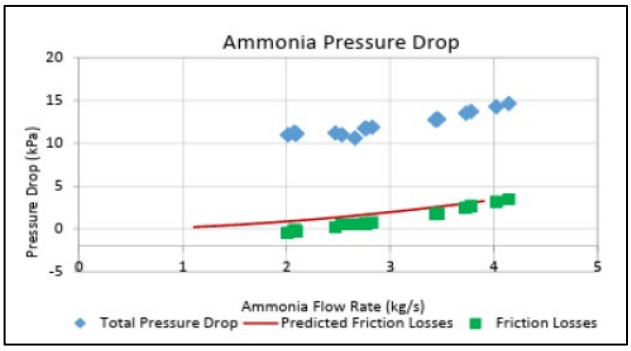

Figure 2: Pressure drop in traditional evaporators in the OTEC [24]

Figure 2 shows the variation of ammonia pressure drop with mass flow rate, where the total pressure drops increases with flow rate and remains significantly higher than the frictional pressure losses predicted by the model.

Moreover, most previous numerical and experimental studies focus on steady-state operation or simplified thermal models, which are insufficient to describe the transient multiphase evaporation behaviour inside compact OTEC evaporators.

This study addresses these limitations through a comprehensive transient CFD simulation of a newly developed multi-channel OTEC evaporator using ANSYS Fluent. The objectives are to evaluate temperature distribution, vapor fraction evolution, and pressure drop under transient conditions, determine the optimal refrigerant mass flow rate, analyse the evaporation behaviour of R-22, and compare the proposed design with a conventional plate heat exchanger. The findings aim to support the development of high-performance, low-pressure-drop evaporators for scalable OTEC applications.

Although ammonia appears to be a newer alternative working fluid for OTEC, the classical R22 often remains a favourable option for its popularity and well understood thermodynamics characteristic. For that reason, this study will focus on R22 as the working fluid, with the findings can later be extrapolated for R717 in future study.

2.0 Literature Review

2.1 OTEC as a Low-Temperature Renewable Energy System

OTEC systems are particularly attractive for tropical and equatorial regions, where the ocean thermal gradient remains stable throughout the year [2]. A commercial-scale 100 MW OTEC plant typically requires a seawater flow rate of 10–20 billion gallons per day, illustrating both the enormous energy potential and the significant engineering challenges associated with seawater handling and heat exchanger design [1]. Beyond electricity generation, OTEC facilities can simultaneously support several secondary applications, including seawater air-conditioning, desalinated freshwater production, aquaculture, and hydrogen generation, thereby improving the overall economic feasibility of the system [3].

Despite its strong theoretical potential, the practical implementation of OTEC remains limited by low thermal efficiency, which is inherently constrained by the small temperature difference available for energy conversion. As a result, the performance of heat exchangers—particularly the evaporator—becomes a dominant factor governing the net power output and economic viability of OTEC plants [2]. Any improvement in evaporator heat transfer efficiency or reduction in pressure losses

directly enhances turbine inlet conditions, reduces pumping power consumption, and increases the overall system efficiency. Therefore, continuous advancements in evaporator design, materials, and flow configuration are essential for the large-scale commercialization of OTEC technology [1,5].

2.2 Importance of Evaporator Performance in OTEC

The evaporator is one of the most critical components in a closed-cycle Ocean Thermal Energy Conversion (OTEC) system, as it directly governs the conversion of low-grade thermal energy from warm surface seawater into mechanical energy at the turbine [4]. In the evaporator, the working fluid absorbs heat and undergoes phase change from liquid to vapor, generating the driving force for the Rankine power cycle. The efficiency of this heat and mass transfer process strongly influences the turbine inlet pressure, vapor quality, and mass flow rate, all of which determine the net power output of the system [1]. Because OTEC operates under a small temperature difference, typically between 20–25 °C, even minor inefficiencies in heat transfer or excessive pressure losses can result in a significant reduction in overall system performance. The evaporator must therefore accomplish three essential tasks simultaneously: (i) achieve near-complete evaporation of the working fluid, (ii) maximize thermal energy absorption from the warm seawater, and (iii) minimize pressure drop across the heat exchanger to reduce pumping power requirements [1]. Failure to satisfy any of these conditions leads to reduced turbine work output and increased parasitic losses within the system [7].

The thermal and hydraulic performance of the evaporator is governed by several interacting parameters, including the heat transfer surface area, flow configuration, channel geometry, working fluid properties, and operating pressure. Inadequate evaporator design may lead to incomplete vaporization, low vapor quality at the turbine inlet, or excessive pressure drop, all of which degrade turbine efficiency and lower cycle performance [5,13,14]. Furthermore, since the evaporator operates continuously in a corrosive marine environment and under sustained thermal loading, its long-term structural integrity and material durability are equally important to ensure reliable plant operation [7].

In practical OTEC systems, the evaporator also contributes significantly to the total system cost due to its large size, for the required heat transfer area. Therefore, improving evaporator effectiveness while simultaneously reducing pressure losses and material usage is a key strategy for enhancing the economic feasibility of OTEC power plants. For these reasons, the development of high-performance, low-pressure-drop evaporators remains a primary research focus in advancing OTEC technology toward commercial viability [15–19].

2.3 Limitations of Plate Heat Exchangers in OTEC Applications

Plate heat exchangers (PHEs) are commonly employed as evaporators in laboratory-scale and pilot OTEC systems due to their compact size and relatively high heat transfer coefficients. However, extensive experimental and operational studies have revealed several critical limitations that restrict their long-term effectiveness and large-scale applicability in OTEC environments [15–20].

One of the major drawbacks of plate heat exchangers is their sealing reliability. The performance of PHEs is strongly dependent on rubber gaskets used to separate fluid streams and prevent leakage [15]. These gaskets are highly susceptible to degradation caused by temperature fluctuations, chemical exposure, improper reconditioning, and non-standard replacement parts. Misaligned or deformed gaskets frequently lead to internal leakage, mixing of fluids, and mechanical failure, resulting in frequent maintenance and increased downtime [15]. Such failures significantly raise operational costs and reduce system availability in continuous OTEC operation.

Another critical limitation is the pressure constraint of PHEs. Due to their reliance on gasketed sealing systems, the maximum allowable operating pressure of PHEs is typically limited to approximately 1–1.5 MPa. This restricts their application in high-pressure OTEC configurations, where elevated refrigerant pressures are required to control boiling temperature and optimize thermodynamic performance [15]. Exceeding these limits increases the risk of leakage and structural failure.

The pressure drop across PHEs also presents a major challenge. Studies have reported pressure drops ranging from 20 to 30 kPa under typical R-22 operating conditions, while in some cases values as high as 20–100 kPa have been observed depending on flow rate, plate spacing, and chevron angle [19]. Experimental studies using ammonia in OTEC plate evaporators have reported pressure drops of approximately 11 kPa under optimized conditions [20]. These pressure losses increase pumping power requirements and reduce the net power output of the OTEC system.

Furthermore, the corrugation angle of plates, which is introduced to enhance turbulence and heat transfer, significantly increases flow

resistance. Plates with higher corrugation angles (e.g., 60°) exhibit much larger pressure drops compared to lower-angle configurations (30°–45°). While turbulence improves heat transfer, the accompanying rise in frictional losses leads to higher energy consumption by circulation pumps [16].

From a thermal performance perspective, plate heat exchangers in OTEC applications generally achieve thermal efficiencies in the range of 10–15%, with heat transfer coefficients typically between 2000 and 3500 W/m²K for R-22 under favourable operating conditions [15–18]. However, this performance is strongly offset by the associated hydraulic losses. In subcritical OTEC cycles using R-22, an overall thermal efficiency of only about 2.92% has been reported when plate evaporators are employed, primarily due to pressure losses and turbine-pump inefficiencies [15].

In addition to thermal–hydraulic limitations, PHEs also face operational challenges in marine environments, including corrosion, biofouling, and structural fatigue. Continuous exposure to seawater accelerates material degradation, while biofouling reduces effective heat transfer surface area and increases pressure drop over time [6–9]. These issues impose strict material requirements and lead to high maintenance costs.

Collectively, the limitations of gasket sealing, pressure resistance, hydraulic losses, thermal inefficiency, and long-term durability significantly constrain the suitability of conventional plate heat exchangers for high-performance and large-scale OTEC applications [26]. These weaknesses strongly justify the development of alternative evaporator designs that can provide enhanced heat transfer performance while maintaining minimal pressure drop and superior mechanical robustness [27].

3.0 METHODOLOGY

3.1 Geometry and Computational Domain

A three-dimensional model of the novel multi-channel OTEC evaporator was developed using SolidWorks and imported into ANSYS Fluent for numerical analysis. The evaporator consists of 24 water channels and 24 refrigerant (R-22) channels arranged in a counterflow configuration. Each refrigerant channel is surrounded by two water channels to maximize heat transfer. To reduce computational cost while preserving physical accuracy, the geometry was symmetrically sliced into representative segments, and results were later radially scaled to predict the full evaporator performance.

The proposed novel heat exchanger configuration is illustrated in Figure 3, showing the overall three-dimensional geometry of the design, while the corresponding geometric parameters, including the number of channels, cylinder length, and inlet area, are summarized in Table 1.

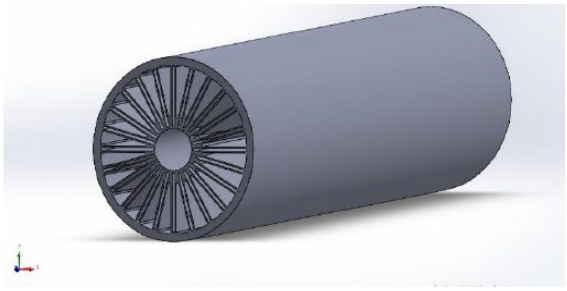

Figure 3: Novel heat exchanger design

Table 1: Novel heat exchanger geometry

Property	Water Channel	R22 Channel
Number of Channels	24	24
Length of Cylinder	500 mm	500 mm
Area (inlet)	54.19 mm²	20.42 mm²

To clarify the internal fluid arrangement and phase interaction, a sectional view of the heat exchanger is presented in Figure 4, highlighting the flow paths of water and R22 within the evaporator.

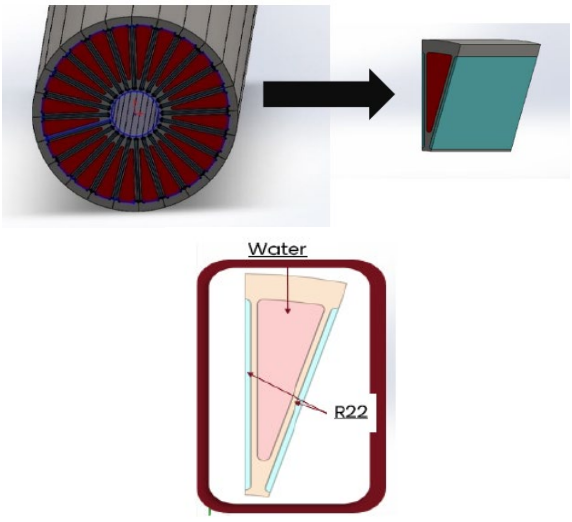

Figure 4: Slice of the heat exchanger for fluid illustration

3.2 Grid Independence and Mesh Quality

Several mesh configurations were tested to establish grid-independent solutions. Table 2 shows the

Model E, with 295,658 elements, strikes an excellent balance between computational efficiency and simulation accuracy. Its significantly lower element count compared to Model N (792,376) and Model Q (771,483) offers faster computation times without compromising on precision.

The orthogonal quality of Model E stands at 0.99789, closely matching Model N's value (0.99512) while outperforming Model Q (0.985652). Skewness values range from 0.33011 to 0.66989, better than Model C and only slightly higher than the more refined Models N and Q, yet well within acceptable limits to maintain high mesh quality. In terms of thermal results, Model E demonstrates convergence, with the R-22 temperature reaching 289.11 K (15.96°C) and the water temperature at 296.69 K. (23.54°C). These values closely align with those observed in Models N and Q, supporting the reliability of its results. Additionally, Model E maintains an element quality rating of 0.96006 and an acceptable aspect ratio, ensuring well-shaped elements suitable for accurate simulations.

The grid independence assessment is presented in Appendix Figure A1, where the predicted outlet temperatures of R22 and water are plotted against the number of mesh nodes. A noticeable variation is observed for coarse grids, while the results stabilize after approximately 295,658 nodes. The corresponding mesh quality parameters and thermal results are detailed in Table 2. Based on these observations, the mesh consisting of 295,658 nodes was adopted for all subsequent simulations to ensure solution accuracy without excessive computational expense.

The numerical error associated with mesh refinement was quantified using the relative error percentage between successive grid resolutions. The error was calculated using the following expression:

$$Error\ (\%) = |(Value\_Model - Value\_Reference) / Value\_Reference| \times 100$$

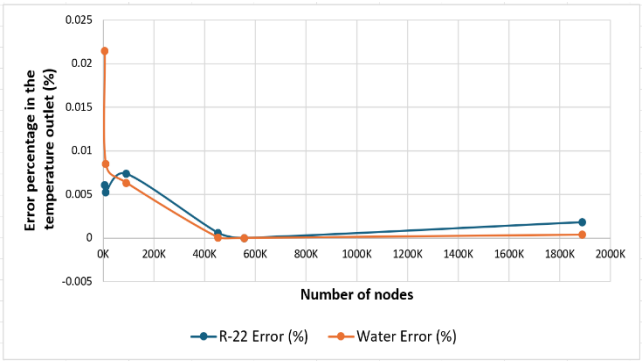

Figure 5: Error percentage in Temperature Outlet

Figure 6 illustrates the variation of error percentage in the outlet temperatures of both R-22 and water with increasing number of mesh elements. At low mesh densities, relatively higher numerical errors were observed due to insufficient spatial resolution. However, as the mesh was progressively refined, the error decreased rapidly and stabilized. It is observed that beyond approximately 300,000 elements, the maximum temperature error for both water and R-22 remains below 0.0025 (0.25%), indicating excellent numerical stability and independence from grid resolution. This confirms that further mesh refinement does not lead to any meaningful change in the outlet temperature predictions. Therefore, the selected mesh density used in the final simulations provides a reliable compromise between computational efficiency and numerical accuracy.

Table 2: Final meshing types for evaluation

Model	Meshing Nodes	Elements	Orthogonal Quality	Skewness (Min / Max)	Aspect Ratio (Min / Max)	Element Quality	R22 Temp (K)	R22 Temp (°C)	Water Temp (K)	Water Temp (°C)
A	5,691	8,029	0.956	0.659	1.862	0.96115	290.69	17.539	290.342	17.192
B	10,103	15,500	0.99406	0.078744	1.5056	0.95137	290.458	17.308	299.232	26.082
C	91,313	119,466	0.98388	0.67595 / 0.32826	0.4381 / 3.6881	0.94137	286.809	13.659	298.591	25.441
M	439,048	659,659	0.98236	0.84669 / 0.52862	0.4381 / 3.6881	0.93982	288.945	15.795	296.642	23.492
E	452,908	295,658	0.99789	0.33011 / 0.66989	1.2719 / 3.1884	0.96006	289.11	15.96	296.69	23.54
N	556,300	792,376	0.99512	0.003112	1.00234/2	0.95523	288.94	15.79	296.71	23.56

Q	1,889,594	771,483	0.985652	0.005637	1.20568 / 2.81445	0.95089	288.419	15.269	296.5	23.35

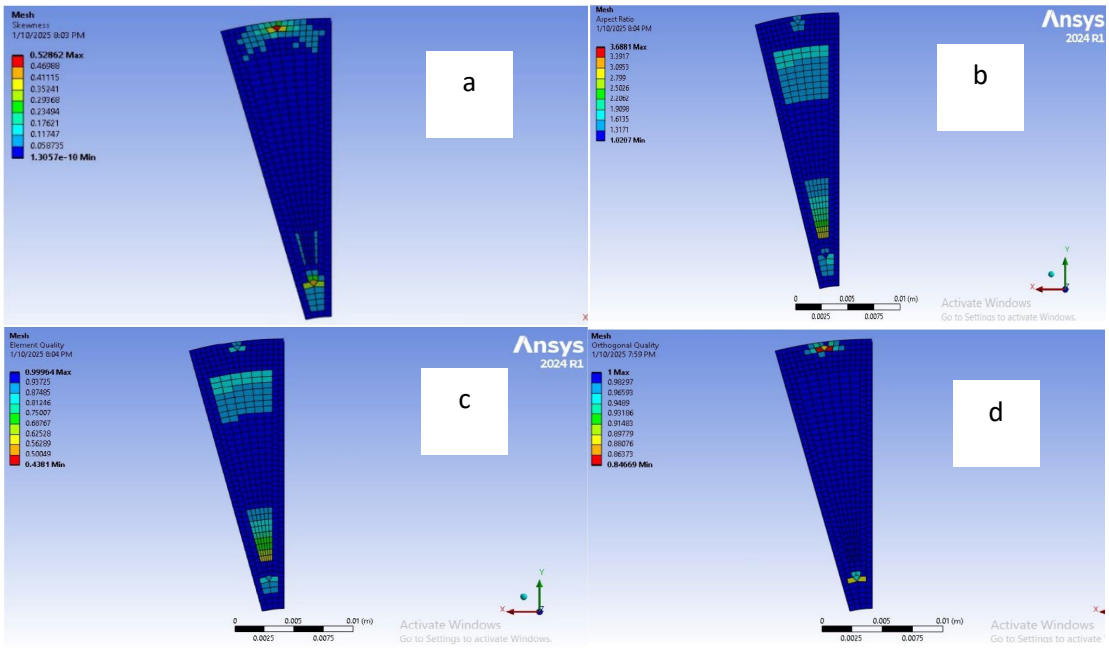

Figure 6: Mesh quality assessment of the computational domain showing (a) skewness distribution, (b) aspect ratio distribution, (c) element quality, and (d) orthogonal quality for the selected grid used in the transient CFD simulations

The mesh quality was quantitatively assessed using skewness, orthogonal quality, aspect ratio, and element quality indicators, as illustrated in Figure 6. The skewness metric, which measures element distortion, remained below 0.21, indicating high-quality cell shapes [21]. Orthogonal quality achieved a value of 0.99789, reflecting excellent alignment of cell faces with predominant flow directions, essential for accurate gradient prediction [21-22]. The average element quality of 0.99964 is consistent with a well-shaped mesh capable of resolving thermal and fluid dynamic gradients effectively.

These values fall well within accepted CFD best-practice criteria (skewness < 0.25; orthogonal quality > 0.9), confirming that the mesh provides a stable, accurate foundation for the transient VOF phase-change simulation. The selected final mesh thus represents an optimal balance between computational cost and numerical accuracy [21-22].

3.3 Boundary Conditions and Multiphase Model

A transient Volume of Fluid (VOF) multiphase model was used to simulate water, air, R22 liquid, and R22 vapor, for its simplicity and its computation efficiency. The fluids are assumed to have clear liquid–vapor interface, and not too strongly dispersed (e.g., in the case of boiling).

Mass-flow inlets and pressure outlets were applied. Gravity was aligned with water flow and opposite to R22 flow direction to match the UTM-LOCARTIC experimental setup. The boundary conditions applied for the numerical simulation are summarized in Table 3 for both the hot fluid (water) and cold fluid (R22).

Table 3: Boundary Conditions

Parameter	Hot Fluid (Water)	Cold Fluid (R22 Liquid)
Mass Flow Rate (kg/s)	1.5	0.0116
Pressure Inlet (kPa)	150	960
Temperature Inlet (°C)	30	5
Pressure Outlet	Variable	Variable
Temperature Outlet	Variable	Variable

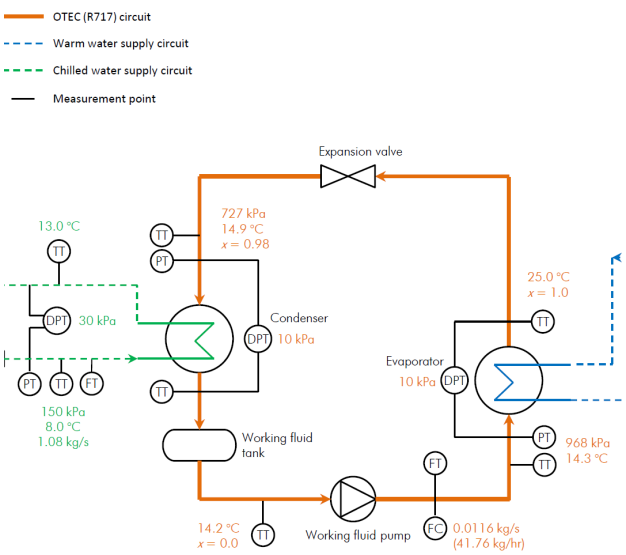

Figure 6: Scaled OTEC Schematic at LOCARTIC

Figure 7 presents the scaled schematic of the OTEC system at LOCARTIC, illustrating the closed loop working fluid circuit together with the warm and cold seawater supply loops.

3.4 Turbulence and Viscosity Models

Simulations were initially run under laminar assumptions, which led to significant numerical divergence. Therefore, k–ε Realizable and k–ω SST models were tested. The k–ω SST model showed superior convergence and better near-wall behaviour. Turbulence kinetic energy distributions for water and R22 are displayed in Figure 8 and Figure 9, confirming laminar behaviour at the inlet and transitional effects during R22 evaporation.

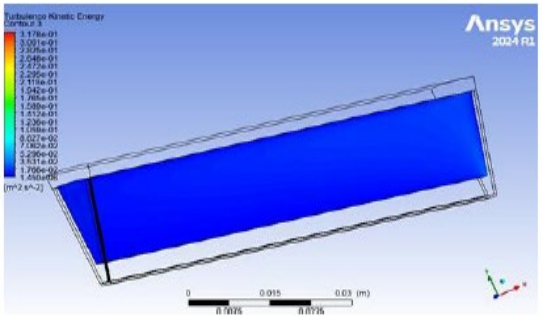

Figure 7: Turbulence kinetic energy for water

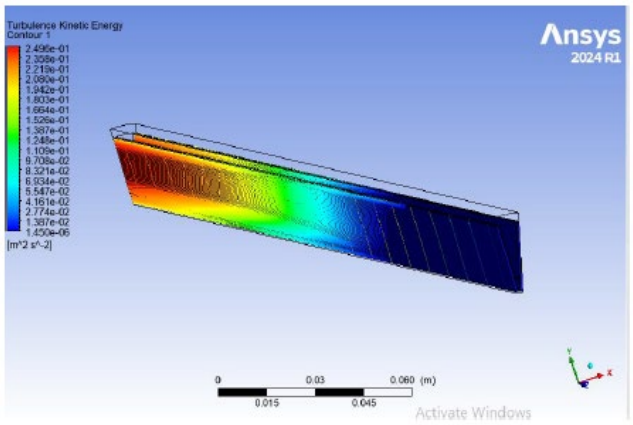

Figure 8: Turbulence kinetic energy for R22

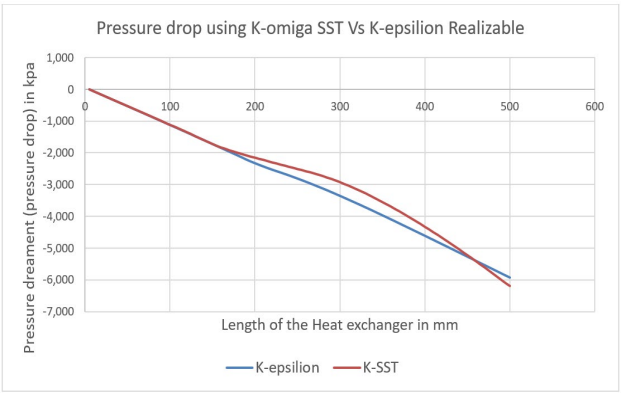

Figure 9: Pressure drop across different viscosity models

A comparison of pressure loss using different models is shown in Figure 10, where the SST k–ω model predicted a realistic maximum pressure drop of 6.19 kPa. For that reason, the SST k–ω model will be employed in this study.

3.5 Lee Evaporation Model

The evaporation frequency represents the rate at which phase change occurs during the boiling/evaporation process. In the absence of experimental validation for the present configuration, the evaporation frequency was adopted from previously reported studies on ammonia flow in geometrically similar tube-shaped heat exchangers for OTEC applications. Accordingly, an evaporation frequency of 40 Hz was used as the reference value. To account for the different thermophysical properties of R22, a conservative assumption was made whereby the R22 bubble diameter was taken to be four times larger than that of ammonia. Since bubble diameter is inversely proportional to evaporation frequency, the evaporation frequency for R22

was therefore reduced by a factor of four. The relationship used for this assumption is given below:

$$\lambda_C = \frac{6}{d_b}\beta\sqrt{\frac{M}{2\pi R T_{sat}}} \times L \times \left(\frac{\alpha_v \rho_v}{\rho_l - \rho_v}\right)$$

Where: d_b = Diameter of bubble (m), β = Adaptation coefficient (Dimensionless), M = Molar mass(kg/mol), T_{sat} = Saturation temperature (K), R = Universal gas constant (J/K-mol), L = Latent heat (J/kg), α_v = Phase volume fraction (Dimensionless), ρ_l = Density of the liquid (kg/m³), ρ_v = Density of the vapor (kg/m³).

Based on the test, the heat exchanger will evaporate 99.99903% of the R22 which is almost 100%, the very small decimal that is still liquid is condensed which indicates that current heat exchanger design is showing great evaporation potential.

3.6 Transient Flow and Time Step Selection

The time step size was determined using the Courant–Friedrichs–Lewy (CFL) condition:

$$\Delta t = \frac{\Delta x \times C}{u}$$

with:
Velocity, u = starting from nominal 0.01957 m/s
Node spacing, Δx = 0.5 mm
CFL coefficient, C = 1

The resulting time step was 0.0255 s for normal flow. Time step adjustments for various mass flow increments are listed in Table 4.

Table 4: Time Step Size at Different R22 Flow Rates

Flow	Velocity (m/s)	Time Step Δt (s)
Normal flow	0.01957	0.0255
+20%	0.02304	0.0217
+40%	0.02651	0.0189
+60%	0.02998	0.0167
+80%	0.03346	0.0150
+100%	0.03693	0.0135

4.0 Results

4.1 Temperature Variation Across the Heat Exchanger

The transient simulation was performed until the outlet temperature of R22 reached a steady state. As shown in Figure 11, the R22 outlet temperature increases rapidly during the initial phase of simulation and stabilizes after approximately 1.8 minutes of flow time. At steady state, the outlet temperature of R22 reaches 27.65 °C, while the outlet temperature of water reaches 29.2 °C.

The temperature distribution along the length of the heat exchanger shows a smooth and continuous heat transfer process between the hot water and the working fluid. The water temperature decreases gradually, while the R22 temperature increases due to heat absorption and phase change. The small temperature drop on the water side is reasonable because the mass flow rate of water is approximately 129 times higher than that of R22, ensuring sufficient thermal energy supply. The resulting thermal efficiency of the evaporator is approximately 24%, which satisfies the thermodynamic consistency of the system. Figure 12 illustrates the temperature variation of R22 outlet.

4.2 Pressure Variation Across the Heat Exchanger

The pressure distribution along the water and R22 channels shown in Figures 13 and 14 indicates a gradual pressure decrease from inlet to outlet. On the water side, the pressure drop is relatively small and remains within the safe operating limits of the system. On the R22 side, a maximum pressure drop of 6.19 kPa was observed at the nominal operating condition.

This pressure drop is significantly lower than that reported for conventional plate heat exchangers used in OTEC systems, which typically exhibit pressure drops exceeding 11 kPa. The reduced pressure loss confirms the effectiveness of the proposed channel configuration in minimizing frictional and acceleration losses. Figure 13 illustrates the pressure variation of water along the length of the heat exchanger.

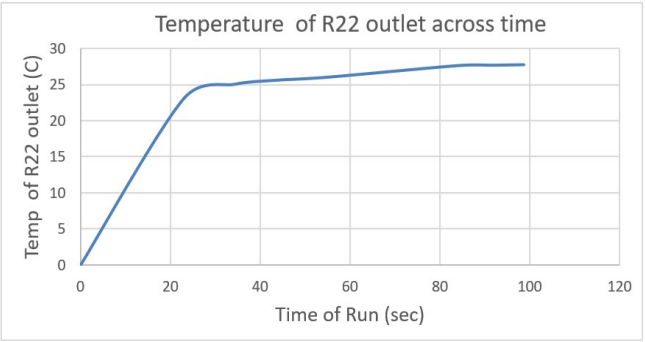

Figure 10: Temperature variation of the R22 outlet increasing the flowtime

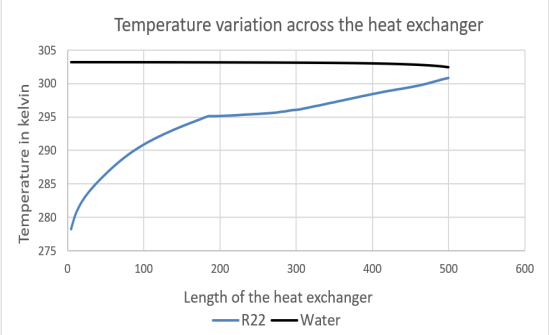

Figure 11: Temperature variation of the R22 outlet and water by increasing the flowtime

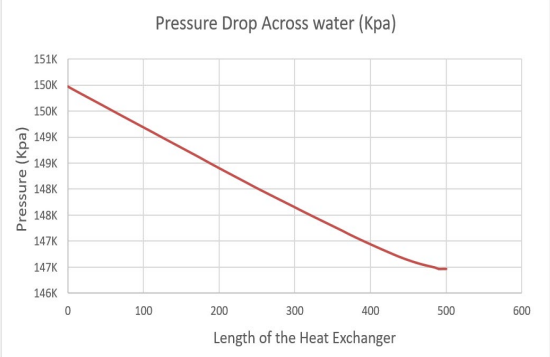

Figure 12: Pressure variation of the water inside the R22 starting from inlet of water

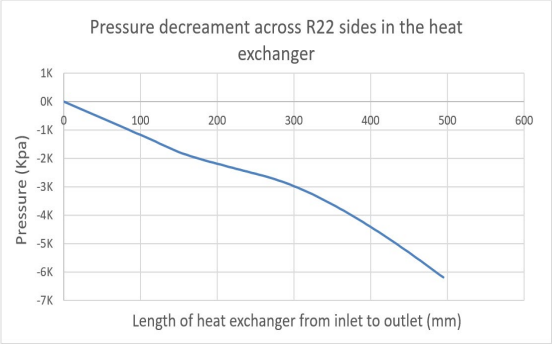

Figure 13: Pressure variation of the R22 inside the heat exchanger starting from inlet of R22

Figure 14 shows the pressure variation of R22 along the length of the heat exchanger from the inlet to the outlet. The pressure decreases continuously along the flow direction, with a more pronounced drop observed toward the outlet region. This nonlinear pressure reduction indicates the combined effects of frictional losses, acceleration, and phase-change phenomena occurring within the R22 channel. The increasing pressure gradient near the outlet suggests intensified vapor generation and flow resistance during the evaporation process.

4.3 Effect of Mass Flow Rate on Pressure Drop

The influence of R22 mass flow rate on pressure drop was investigated by increasing the inlet mass flow rate from the nominal value up to 100% increment. The results show that the pressure drop increases monotonically with increasing mass flow rate, reaching a maximum value of 8.47 kPa at the highest flow condition.

An optimal operating mass flow rate of 0.01856 kg/s was identified, at which the pressure increment remains minimal while still providing high thermal absorption. Beyond this value, the pressure drops increases more rapidly, leading to higher pumping power requirements. This confirms that 0.01856 kg/s represents the most economical operating condition for the evaporator.

Figure 15 illustrates the pressure variation of R22 along the length of the heat exchanger at different inlet mass flow rates. For all flow conditions, the pressure decreases continuously from the inlet to the outlet, indicating progressive frictional and momentum losses along the channel. It is observed that higher mass flow rates result in a greater pressure drop, particularly near the outlet region, due to the increased flow resistance and enhanced two-phase interaction.

This trend is further confirmed in Figure 16, which shows that the total pressure drop across the R22 side increases monotonically with increasing mass flow rate. The rising pressure drop with flow rate reflects the dominant influence of viscous and acceleration effects during the evaporation process.

4.4 Vapor Fraction and Evaporation Performance

Figure 17 shows Rate of evaporation at different flowrates. The vapor volume fraction distribution along the R22 channel demonstrates that the novel evaporator can achieve complete evaporation of liquid R22 under all tested flow conditions. The vapor fraction increases progressively along the channel length and reaches a value of nearly 1.0, indicating 100% vaporization.

At the nominal operating condition, the Lee evaporation model predicts an evaporation efficiency of 99.99903%, with only a negligible fraction of liquid R22 remaining. This confirms the strong heat transfer and phase-change capability of the proposed evaporator design [23].

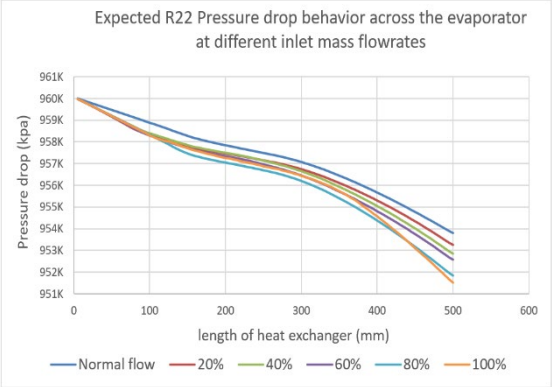

Figure 14: Pressure variation of the R22 inside the heat exchanger

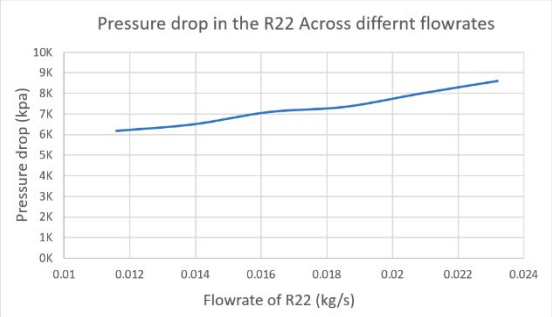

Figure 15: Relation between the mass flowrate and the pressure drop

Table 5: Performance Comparison Table

Performance Indicator	Novel Heat Exchanger	Plate Heat Exchanger
Outlet temperature of R22	27.65 °C	26 °C
Outlet temperature of water	29.265 °C	27 °C
Thermal energy lost from water	10.15 kW	18 kW
Thermal energy absorbed by R22	2.45 kW	2.43 kW
Thermal efficiency (evaporator)	24%	13.5%
LMTD	8.9 °C	10.55 °C
NTU	2.143	2
Effectiveness (NTU)	88.2%	86%
Pressure drops in R22	6.19 kPa	11 kPa

4.5 Overall Performance of the Novel Heat Exchanger

The thermal and hydraulic performance of the proposed evaporator was compared with a conventional plate heat exchanger scaled to match the LOCARTIC-OTEC laboratory system. The comparison is given in Table 5.

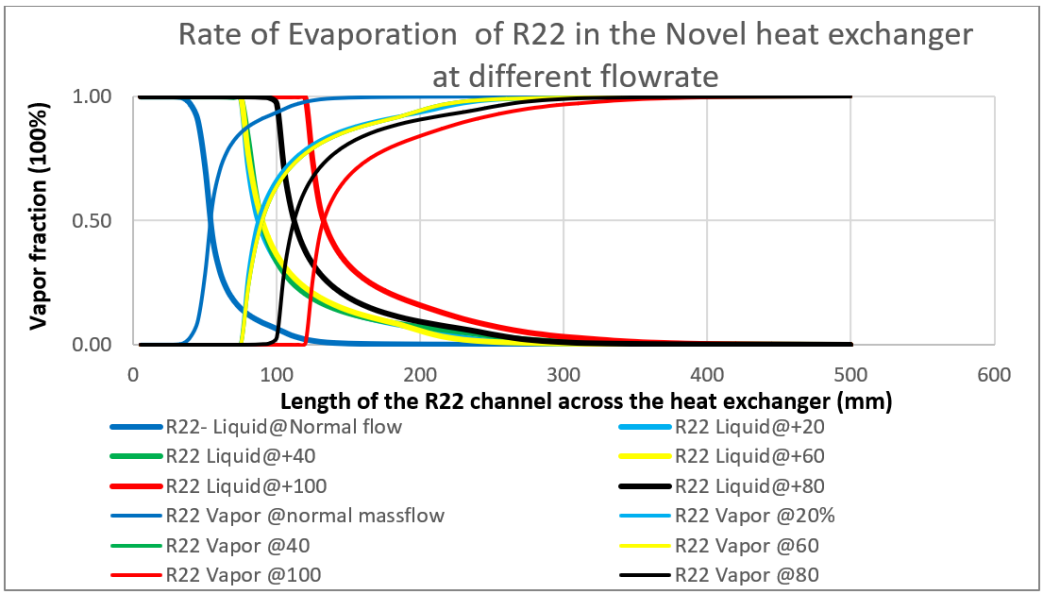

Figure 16: Rate of evaporation at different flowrates

In comparison, the plate heat exchanger exhibits a lower thermal efficiency of 13.5% and a higher-pressure drop of 11 kPa. The novel evaporator therefore demonstrates superior thermal performance with significantly reduced pressure losses,

making it more economical and suitable for OTEC applications.

Based on the optimal flow rate of 0.01856 kg/s, the resulting specific thermal energy absorbed by the working fluid using the new concept heat exchanger would be 132 kJ/kg. In real-world OTEC plant design, the evaporator heat exchanger may be sized according to this specific performance to match the desired plant capacity.

5.0 Conclusion

This study presented a transient CFD analysis of a novel evaporator designed for Ocean Thermal Energy Conversion (OTEC) applications. The simulation results confirm that the proposed evaporator can achieve complete evaporation (100%) of liquid R22 while maintaining a maximum pressure drop of only 6.19 kPa under nominal operating conditions. The pressure drop was found to increase with increasing mass flow rate, reaching a maximum value of 8.6 kPa at a 100% flow increment, which remains significantly lower than the typical values reported for conventional plate heat exchangers.

The absorbed thermal energy was observed to increase with mass flow rate, reaching 3.9 kW at a 60% increment and 4.9 kW at a 100% increment, indicating strong heat transfer capability. An optimal operating mass flow rate of 0.01856 kg/s was identified, which provides a favourable balance between heat absorption and pressure drop when compared to the initial flow rate of 0.0116 kg/s. The transient temperature analysis further showed that the R22 outlet temperature reaches approximately 27.85 °C within 1.6 minutes, confirming rapid thermal stabilization.

Scaling analysis indicates that the proposed heat exchanger could increase the thermal energy absorbed by approximately 2 kW when applied to a full-scale OTEC plant reported in the literature. Based on the overall thermal and hydraulic performance, the simulation results demonstrate that the novel evaporator meets the operational requirements of OTEC systems. The evaporator is therefore technically valid for fabrication, and experimental testing is strongly recommended as the next stage to validate the numerical predictions and support real-world deployment.

5.1 Future work

Future work shall focus on enhancing heat transfer by introducing controlled turbulence at the inlets of both water and R22, made possible by the low-pressure drop of the present design. This may be achieved by adding surface scratches, small internal tunnels, or simple flow-disturbing elements such as horizontal rods to improve flow mixing, accelerate boiling, and reduce the evaporation length to below 200 mm. Experimental validation of the CFD model is also essential by testing different mass flow rates and measuring pressure drops and turbine output to confirm whether, at the optimal R22 flow rate of 0.01856 kg/s, the turbine power exceeds the pumping power. In addition, the gasket-free structure of the novel heat exchanger enables the introduction of a new hybrid concept, namely Solar–Ocean Thermal Energy Conversion (Solar-OTEC), where solar energy from Fresnel lenses or concentrated solar collectors can be used to increase seawater temperature to 60–90°C or higher. With further enhancement, direct boiling of water above 120°C may be achievable without using refrigerants, offering a promising solution for low-temperature regions such as middle East.

Acknowledgement

The author would like to acknowledge the Ministry of Higher Education Malaysia (MoHE) for funding this research –under the registered program cost centre: #R.J130000.7809.4L893

References

[1] Masutani, S. M., & Takahashi, P. K. (2001). Ocean thermal energy conversion (OTEC). In J. H. Steele, S. A. Thorpe, & K. K. Turekian (Eds.), Encyclopedia of Ocean Sciences (pp. 1993–1999). Elsevier. https://doi.org/10.1006/rwos.2001.0031

[2] Sanjivy, K., Raybaud, P., Hunt, J., Ferrucci, F., Baucour, P., Marc, O., & Lucas, F. (2026). Harnessing the ocean's depths: SWAC and OTEC for sustainable cooling and power – A review of technologies, applications and challenges. Renewable and Sustainable Energy Reviews, 226(A), 116253. https://doi.org/10.1016/j.rser.2025.116253

[3] Jing, F., Wang, X., Mei, Y., & Tian, R. (2025). A comprehensive review on ocean thermal energy conversion technology: Thermodynamic optimization, multi-energy integration, and byproduct utilization. Energy Conversion and Management: X, 27, 101188. https://doi.org/10.1016/j.ecmx.2025.101188

[4] Tinakar, A. (2013). Ocean thermal energy conversion. International Journal of Energy and Power Engineering, 2(4), 143. https://doi.org/10.11648/j.ijepe.20130204.11

[5] Wu, Z., Feng, H., Chen, L., Xie, Z., & Cai, C. (2019). Pumping power minimization of an evaporator in ocean thermal energy conversion system based on constructal theory. Energy, 181, 974–984. https://doi.org/10.1016/j.energy.2019.05.216

[6] Musabikha, S., & Utama, I. K. A. P. (2017). Corrosion in the marine renewable energy: A review. International

Journal of Environmental Research and Clean Energy, 7(1). http://isomase.org/IJERCE1.php

[7] Zhang, W., Li, Y., Wu, X., & Guo, S. (2018). Review of the applied mechanical problems in ocean thermal energy conversion. Renewable and Sustainable Energy Reviews. https://doi.org/10.1016/j.rser.2018.05.048

[8] Abidin, M. Z. Z., Rodhi, M. N. M., Hamzah, F., & Ghazali, N. A. (2021). Assessing biofouling in ocean thermal energy conversion (OTEC) power plant – A review. In Journal of Physics: Conference Series (Vol. 2053, No. 1, p. 012011). IOP Publishing. https://doi.org/10.1088/1742-6596/2053/1/012011

[9] Adie, P. W., et al. (2023). Non-linear assessment of cold-water pipe (CWP) on the ocean thermal energy conversion (OTEC) installation under bending load. Procedia Structural Integrity, 142–149. https://doi.org/10.1016/j.prostr.2023.07.005

[10] Zhang, J., Zhang, X., Zhang, Z., Zhou, P., Zhang, Y., & Yuan, H. (2022). Performance improvement of ocean thermal energy conversion organic Rankine cycle under temperature glide effect. Energy, 246, 123440. https://doi.org/10.1016/j.energy.2022.123440

[11] Chan, W. L., & Chiong, M. S. (2023). A performance study of R717 and R22 as the working fluid for OTEC plant. In IOP Conference Series: Earth and Environmental Science (Vol. 1143, No. 1, p. 012018). https://doi.org/10.1088/1755-1315/1143/1/012018

[12] Patil, P. M., Yadav, A. P., & Patil, P. A. (2015). Comparative study between heat transfer through laminar flow and turbulent flow. International Journal of Innovative Research in Science, Engineering and Technology, 4(4). https://doi.org/10.15680/IJIRSET.2015.0404076

[13] AIChE. (2018). The essentials of continuous evaporation. https://www.aiche.org/cep

[14] Ma, Q., et al. (2023). Performance improvement of OTEC-ORC and turbine based on binary zeotropic working fluid. International Journal of Chemical Engineering, 2023, Article 8892450. https://doi.org/10.1155/2023/8892450

[15] Yasunaga, T., Miyazaki, A., Fontaine, K., & Ikegami, Y. (n.d.). Comprehensive heat exchanger performance evaluation method on ocean thermal energy conversion for maximum net power. Unpublished technical paper

[16] Rao, B. S., Krishna, M. M., Sastry, R. C., Professor, A., & Student, P. (2014). Experimental studies on pressure drop in a sinusoidal plate heat exchanger: Effect of corrugation angle. http://www.iirct.org

[17] Ikegami, Y., Mutair, S., & Kawabata, Y. (2015). Experimental and numerical investigations on plate-type heat exchanger performance. Open Journal of Fluid Dynamics, 5(1), 92–98. https://doi.org/10.4236/ojfd.2015.51011

[18] Peng, J., Chen, F., Liu, L., Ge, Y., Wu, H., & Liu, W. (2020). Experimental research on plate heat exchanger in OTEC system. Journal of Applied Science and Engineering, 23(1), 21–29. https://doi.org/10.6180/jase.202003_23(1).0003

[19] Yoon, J. I., Son, C. H., Baek, S. M., Kim, H. J., & Lee, H. S. (2014). Efficiency comparison of subcritical OTEC power cycle using various working fluids. Heat and Mass Transfer, 50(7), 985–996. https://doi.org/10.1007/s00231-014-1310-8

[20] Xiao, C., & Gulfam, R. (2023). Opinion on ocean thermal energy conversion (OTEC). Frontiers in Energy Research. https://doi.org/10.3389/fenrg.2023.1115695

[21] Versteeg, H. K., & Malalasekera, W. (2007). *An introduction to computational fluid dynamics: The finite volume method* (2nd ed.). Pearson Education.

[22] Adam, N. M., Attia, O., Al-Sulttani, A. O., & Mahmood, H. A. (2020). Numerical analysis for solar panel subjected with an external force to overcome adhesive force in desert areas. CFD Letters, 12(9), 60–75. https://doi.org/10.37934/cfdl.12.9.6075

[23] Rathore, S. S., Mehta, B., Kumar, P., & Asfer, M. (2023, December). *Numerical validation of Lee's evaporation model for heat pipe applications* [Poster]. Indian Institute of Technology Bhilai; Indian Institute of Technology Mandi; Shaqra University.

[24] Rocheleau, R. E. (2014). Asia Pacific Research Initiative for Sustainable Energy Systems 2011 (APRISES11) OTEC heat exchanger development and testing task 4.1 (Report No. AD1040493). Defense Technical Information Center.

[25] Abu-Khader, M. M. (2012). Plate heat exchangers: Recent advances. Renewable and Sustainable Energy Reviews, 16(4), 1883–1891. https://doi.org/10.1016/j.rser.2012.01.009

[26] Martins, G., Zanzi, M., Oliveira, J. L. G., & De Paiva, K. V. (2024). Structural analysis and sealing capacity of gasketed plate heat exchangers with HNBR and EPDM rubbers. Journal of the Brazilian Society of Mechanical Sciences and Engineering, 46(10), 602. https://doi.org/10.1007/s40430-024-05183-4

[27] Yasunaga, T., Noguchi, T., Morisaki, T., & Ikegami, Y. (2018). Basic heat exchanger performance evaluation method on OTEC. Journal of Marine Science and Engineering, 6(2), 32. https://doi.org/10.3390/jmse6020032

APPENDIX

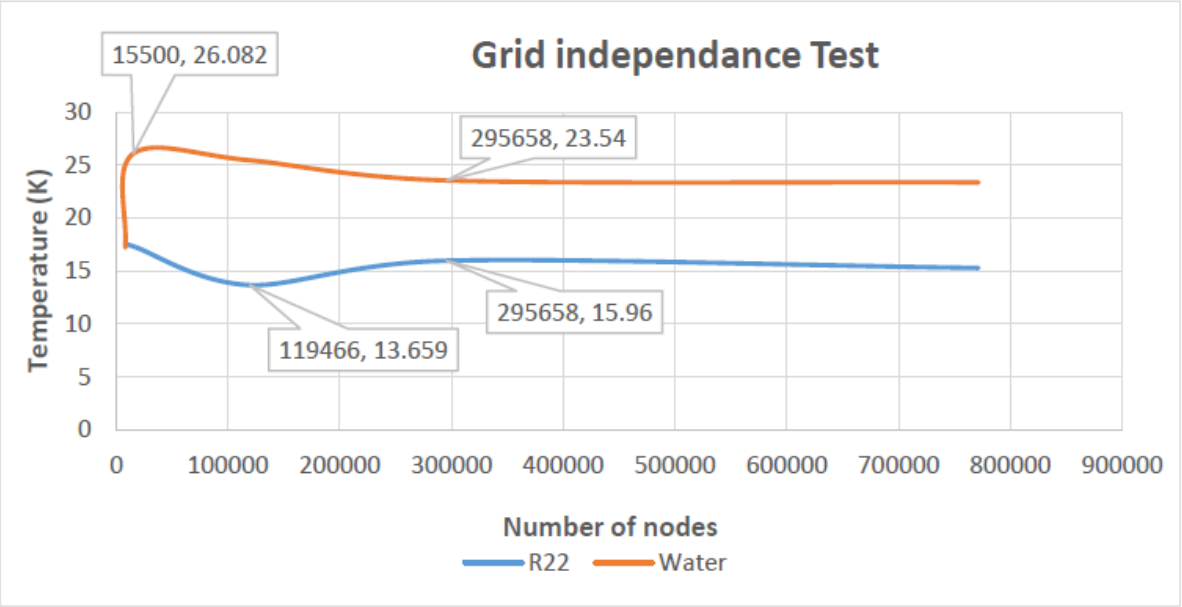

Figure A1: Grid independent test